Crystal Orientation Changes in Two-Dimensionally Confined Nanocylinders in a Poly(ethylene oxide)-*b*-polystyrene/Polystyrene Blend

Ping Huang, Lei Zhu, Stephen Z. D. Cheng,* Qing Ge, and Roderic P. Quirk

Maurice Morton Institute and Department of Polymer Science, The University of Akron, Akron, Ohio 44325-3909

Edwin L. Thomas

Department of Materials Science and Engineering, Massachusetts Institute and Technology, Cambridge, Massachusetts 02139

Bernard Lotz

Institute Charles Sadron, 6 Rue Boussingault, Strasbourg 67083, France

Benjamin S. Hsiao, Lizhi Liu, and Fengji Yeh

Department of Chemistry, The State University of New York at Stony Brook, Stony Brook, New York 11794-3400

Received April 17, 2001; Revised Manuscript Received July 2, 2001

ABSTRACT: A lamella-forming poly(ethylene oxide)-*b*-polystyrene (PEO-*b*-PS) diblock copolymer has been blended with a low molecular weight polystyrene (PS) homopolymer to form a miscible polymer blend. The PEO volume fraction is 0.32, and the order−disorder transition temperature (T_{ODT}) of this blend is 175 °C. Therefore, the PEO blocks form nanocylinders surrounded by a PS matrix below the T_{ODT}. Since the glass transition temperature of the PS is 64 °C and the PEO crystal melting occurs at ∼50 °C, the PEO-block crystallization takes place in a two-dimensionally confined glassy environment. The cylinder diameter is determined to be 13.7 nm, based on small-angle X-ray scattering (SAXS) and transmission electron microscopy results. Using simultaneous two-dimensional SAXS and wide-angle X-ray scattering techniques, the crystal orientation (the *c*-axes of the PEO crystals) within the nanocylinders is found to change simply depending upon the crystallization temperature (T_c). At very low T_c (<−30 °C), PEO crystals are randomly oriented within the confined cylinders. Starting at $T_c = -30$ °C, the crystal orientation changes to be inclined with respect to the cylinder axis, $\hat{a}$. The tilt angle from $\hat{a}$ continuously increases with increasing T_c, and finally it becomes 90° when $T_c \geq 2$ °C. Crystallographic analysis indicates that the crystal *c*-axis orientation at each T_c corresponds to a uniform crystal orientation.

Introduction

In the past decade, crystal orientation tailored by ordered phase morphology in a nanometer length scale, using crystalline−amorphous block copolymers, has received substantial attention. The simplest confinement geometry is the one-dimensionally (1D) confined lamellae in crystalline−amorphous block copolymers. Under this 1D confinement, various crystal orientations (usually the *c*-axes of crystals) were observed. For example, the crystal *c*-axes were observed to be either parallel (homeotropic)[1−5] or perpendicular (homogeneous)[6−11] to the lamellar surface normal ($\hat{n}$). In some particular samples, the crystal *c*-axes were inclined to $\hat{n}$.[12−14] Different crystal orientations were speculated to be associated with different chemical structures of block copolymers and/or different molecular weights.[10]

Recently, we reported our observations on the crystallization temperature (T_c)-dependent crystal orientations in 1D confined nanolamellae in a poly(ethylene oxide)-*b*-polystyrene (PEO-*b*-PS, $\bar{M}_n^{PEO} = 8.7$K g/mol and $\bar{M}_n^{PS} = 9.2$K g/mol) diblock copolymer.[15] Since the glass transition temperature of the PS blocks ($T_g^{PS} = 62$ °C) was higher than the melting temperature of PEO crystals ($T_m^{PEO} \sim 51$ °C when $T_c < 40$ °C) and the order−disorder transition temperature of this diblock copolymer ($T_{ODT} = 160$ °C) was higher than both the T_g^{PS} and T_m^{PEO}, the PEO-block crystallization was observed to be confined between the neighboring glassy PS layers (i.e., in the case of $T_{ODT} > T_g^{PS} > T_c^{PEO}$ [16]). Four T_c regions were recognized on the basis of simultaneous two-dimensional (2D) small-angle and wide-angle X-ray scattering (SAXS and WAXS) experiments on the shear-oriented samples. First, for $T_c < -50$ °C the PEO crystals were randomly oriented. Second, between -50 °C $\leq T_c \leq -10$ °C the *c*-axes of the PEO crystals were oriented perpendicular to $\hat{n}$. Third, when -5 °C $\leq T_c \leq 30$ °C, the *c*-axes of the PEO crystals were inclined to $\hat{n}$. The *c*-axis tilt angle with respect to the lamellar surface increased with increasing T_c. Finally, for $T_c \geq 35$ °C the *c*-axes of the PEO crystals were parallel to $\hat{n}$. It was also found that specific crystal orientation was not determined by the preorientation of primary nuclei, but by an early stage crystal growth in the 1D-confined nanospace.[17]

Crystal orientations in 2D-confined nanocylinders are also of interest using crystalline−amorphous diblock copolymers. A series of polyethylene (PE)-*b*-poly(3-methyl-1-butane) diblock copolymers with different molecular weights and a PE-*b*-poly(vinylcyclohexane) (PE-*b*-PVCH) diblock copolymer were investigated.[18,19] Crystallization of the PE blocks in various block copoly-

* To whom correspondence should be addressed. E-mail: cheng@polymer.uakron.edu.

10.1021/ma010671x CCC: $20.00
Published on Web 08/14/2001

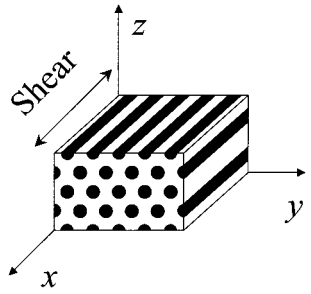

Figure 1. Schematic of the shear geometry for the PEO-*b*-PS/PS blend sample.

mers was observed to be confined within cylindrical morphologies, and the *c*-axes of PE crystals were found either perpendicular to the cylinder axes ($\hat{a}$) or slightly tilted (less than 30°) from this perpendicular direction under different thermal histories.[18,19] Crystal orientation directed by hexagonal cylinders of the amorphous blocks in the inverse cylinder phase was also investigated in PE-containing and other crystalline−amorphous block copolymers.[20,21,23] The *b*-axes of PE crystals were oriented more or less parallel to $\hat{a}$.[21,23] The *c*-axes of PE crystals were perpendicular to the $\hat{a}$ in a PE-*b*-poly(ethylene-*alt*-propylene)-*b*-PS terpolymer,[21] while they were proposed parallel to the {1010} planes of the hexagonal cylinders in PE-*b*-PS and PE-*b*-PVCH block copolymers.[23]

To systematically study the crystal orientation in 2D-confined nanocylinders, a lamella-forming PEO-*b*-PS (8.7K−9.2K) diblock copolymer is blended with a PS homopolymer ($\bar{M}_n$ = 4.6K), and the overall PEO volume fraction is controlled to be 0.32. Since the $\bar{M}_n$ of the PS homopolymer is lower than that of the PS blocks in PEO-*b*-PS, they form a miscible blend.[24] The phase morphology thus shifts to the hexagonal packed nanocylinders formed by the PEO blocks in the PS matrix. The T_{ODT} of this cylindrical structure in the blend has been determined using 1D SAXS experiments at different temperatures, and it is at 175 °C. The T_g^{PS} of this blend is 64 °C as measured by differential scanning calorimetry, and it is higher than the T_m^{PEO} (∼50 °C when T_c < 40 °C) of the PEO crystals.[25] This meets the criteria of a hard confinement case on the PEO crystallization: $T_{ODT} > T_g^{PS} > T_c^{PEO}$, and the PEO-block crystallization occurs within 2D-confined cylinders.[16] The macroscopically oriented blend samples were obtained by planar mechanical shear. Simultaneous 2D SAXS and WAXS experiments were used to investigate different crystal orientations within the 2D-confined nanocylinders at various T_c.

Experimental Section

Materials and Sample Preparation. The PEO-*b*-PS diblock copolymer was synthesized via sequential anionic block copolymerization of styrene and ethylene oxide. The synthesis procedures can be found elsewhere.[26,27] The PS precursor was characterized by size exclusion chromatography (SEC) using polystyrene standard and had an $\bar{M}_n$ of 9.2K and a polydispersity of 1.02. The $\bar{M}_n$ of the PEO blocks was determined by proton nuclear magnetic resonance (^{1}H NMR) to be 8.7K, and the polydispersity of 1.04 in the final diblock copolymer was determined by SEC using the universal calibration. The $\bar{M}_n$ of the PS homopolymer was also characterized by SEC with PS standards, and an $\bar{M}_n$ of 4.6K and a polydispersity of 1.05 were observed. The volume fraction of PEO blocks was purposely set at 0.32 in the melt at 60 °C. (The densities of amorphous PEO and PS are 1.092 and 1.035 g/cm^3.[27])

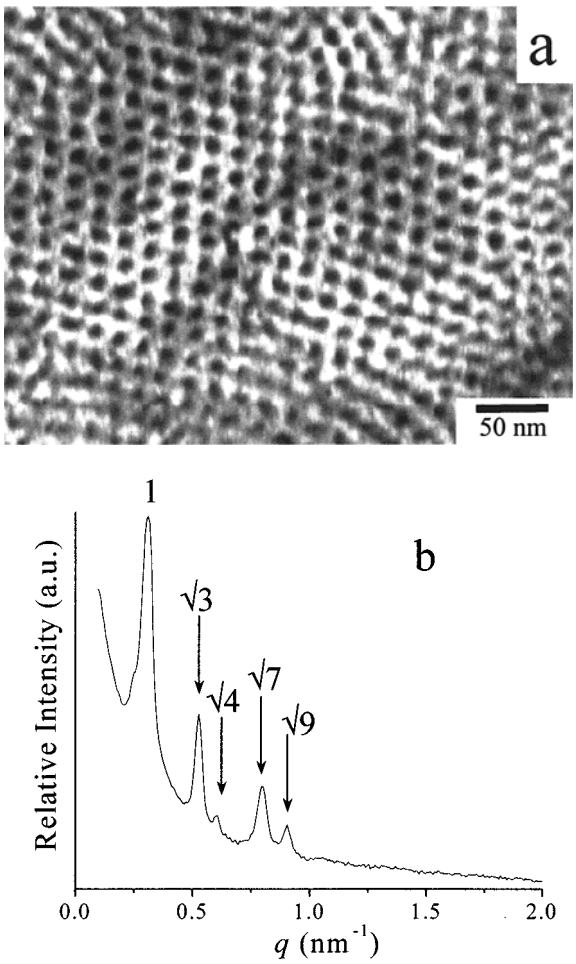

Figure 2. Bright field TEM micrograph of a head-on view of the cylinder phase morphology after the sample is stained by RuO_4 (a) and a 1D SAXS pattern of hexagonal cylinders for the unoriented sample (b).

To ensure the consistency of the phase behavior, uniform sample preparation procedure and identical thermal history were necessary. The blend sample was cast from a 5% (w/v) toluene solution, and the solvent was allowed to evaporate slowly under a dry nitrogen atmosphere at 50 °C to prevent the crystallization of the PEO blocks. Residual solvent was removed under vacuum at 50 °C for 1 day, and the sample was then annealed at 95 °C for 12 h to allow the development of microphase separation. To study the crystal orientation in this blend, the microphase-separated sample was subjected to a large-amplitude oscillating shear (LAOS) under a dry argon atmosphere at 110 °C to achieve uniform alignment of the cylindrical phase morphology. The apparatus was set up in our laboratory, which included a fixed bottom base with a hot stage and a mobile top plate. Mechanical motion of the top plate was controlled by a motor. The shear frequency was 0.5 Hz, and the shear amplitude was 150%. The shear-aligned sample was further annealed at 95 °C for another 12 h in a vacuum to eliminate any residual stresses.

Equipment and Experiments. Simultaneous 2D SAXS and WAXS experiments were conducted at the synchrotron X-ray beam-line X27C at the National Synchrotron Light Source in Brookhaven National Laboratory. The wavelength of the X-ray beam was λ = 0.1307 nm. The zero pixel of the 2D SAXS pattern was calibrated using silver behenate, with the first-order scattering vector q^* ($q^* = 4\pi \sin\theta/\lambda$, where 2θ is the scattering angle) being 1.076 nm^{-1}. 2D WAXS was calibrated using α-Al_2O_3 with known crystal diffractions and air scattering being subtracted. Azimuthal profiles for 2D WAXS patterns were obtained via scans, which were started

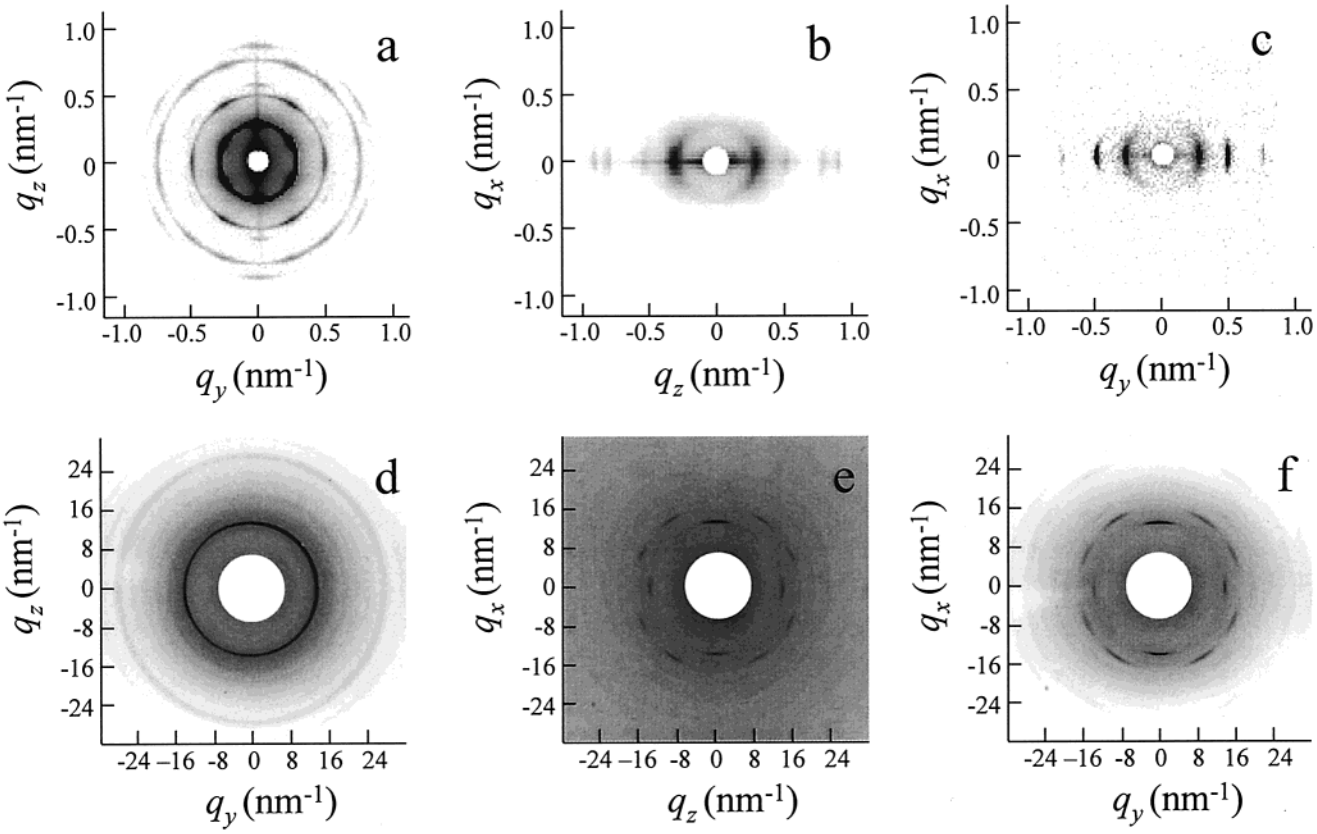

Figure 3. X-ray scattering patterns of shear-aligned samples isothermally crystallized at 30 °C. (a) A 2D SAXS pattern when the X-ray beam is parallel to *x*; (b) a 2D SAXS pattern when the X-ray beam is parallel to *y*; (c) a 2D SAXS pattern when the X-ray beam is parallel to *z*; (d) a 2D WAXS pattern when the X-ray beam is parallel to *x*; (e) a 2D WAXS pattern when the X-ray beam is parallel to *y*; (f) a 2D WAXS pattern when the X-ray beam is parallel to *z*.

on the vertical direction of the patterns. The standard deviation in determining the angular maximum is ±3°.

Isothermal crystallization experiments of PEO-blocks were conducted using an Instec LN2-P2 hot stage equipped with a liquid nitrogen cooling system. The isothermal T_c was controlled to within ±0.2 °C. The shear-aligned samples were preheated to 70 °C for 3 min and then quickly quenched (switched) to the hot stage at a preset T_c for crystallization. The lower limit of the isothermal T_c, which was controllable, was −50 °C.

Transmission electron microscopy (TEM, JEOL 1200 EX II) experiments were carried out at an accelerating voltage of 120 kV. Thin sample sections were obtained using a Reichert Ultracut S (Leica) microtome at −40 °C to cut the shear-aligned samples perpendicular to the shear direction. The samples were stained using RuO_4 vapor at room temperature for 20 min.[28]

Results and Discussion

Cylindrical Phase Morphology of the Shear-Aligned Samples. The shear geometry of the blend sample is shown in Figure 1. The shear direction is along *x*, and *xy* is the shear plane with the shear gradient direction along *z*. The bright-field TEM micrograph of a thin section of the shear-aligned PEO-*b*-PS/PS blend sample after RuO_4 staining is shown in Figure 2a. Since PEO blocks are easier to be stained by RuO_4 than PS, the PEO cylinders appear darker than the PS matrix. The cutting direction of the sample is roughly perpendicular to the shear (the *x*) direction, and thus, the TEM micrograph in Figure 2a is a head-on view of the hexagonal cylinder morphology. Figure 2b shows a 1D SAXS curve of an unoriented sample, which clearly indicates a hexagonal cylinder morphology having $q/q^* = 1{:}\sqrt{3}{:}\sqrt{4}{:}\sqrt{7}{:}\sqrt{9}$ (where q^* is the scattering vector of the first-order reflection). The distance between neighboring centers of the cylinders is 23.1 nm, and each cylinder diameter is calculated to be 13.7 nm on the basis of SAXS, the volume fraction of PEO blocks, and TEM results.

Figure 3 shows simultaneous 2D SAXS and WAXS results of the shear oriented PEO-*b*-PS/PS blend sample when the X-ray beam is along the *x* (Figure 3a,d), the *y* (Figure 3b,e), and the *z* (Figure 3c,f) directions, respectively, after the sample was isothermally crystallized at 30 °C. There are five orders of SAXS reflections in Figure 3a when the X-ray beam is along the *x* direction. They are the $(10\bar{1}0)$, $(1\bar{2}10)$, $(20\bar{2}0)$, $(21\bar{3}0)$, and $(30\bar{3}0)$ reflections of the hexagonal phase. The relationship of these reflections is $q/q^* = 1{:}\sqrt{3}{:}\sqrt{4}{:}\sqrt{7}{:}\sqrt{9}$. The 6-fold symmetry in this pattern clearly indicates that the cylinders in the blend are packed into a hexagonal lattice. In Figure 3a, it is observed that a pair of the $[10\bar{1}0]$ directions is perpendicular to the shear plane (the *xy* plane). Therefore, the $(10\bar{1}0)$ planes of the hexagonal lattice are oriented parallel to the *xy* plane, which are similar to the results of previous reports.[19,22,23,29] Parts b and c of Figure 3 are side-view SAXS patterns with the X-ray beam aligned to the apex and the side of the hexagonal lattice, respectively. Strictly speaking, if the hexagonal lattice is perfectly oriented with the $(10\bar{1}0)$ planes parallel to the *xy* plane, only the $(10\bar{1}0)$, $(20\bar{2}0)$, and $(30\bar{3}0)$ reflections should be observed when the X-ray is aligned to the apex (the *y* direction). Meanwhile, only the $(1\bar{2}10)$ reflection should appear if the X-ray is aligned to the side (the *z* direction). However, several orders of reflections with $q/q^* = 1{:}\sqrt{3}{:}\sqrt{4}{:}\sqrt{7}{:}\sqrt{9}$ are

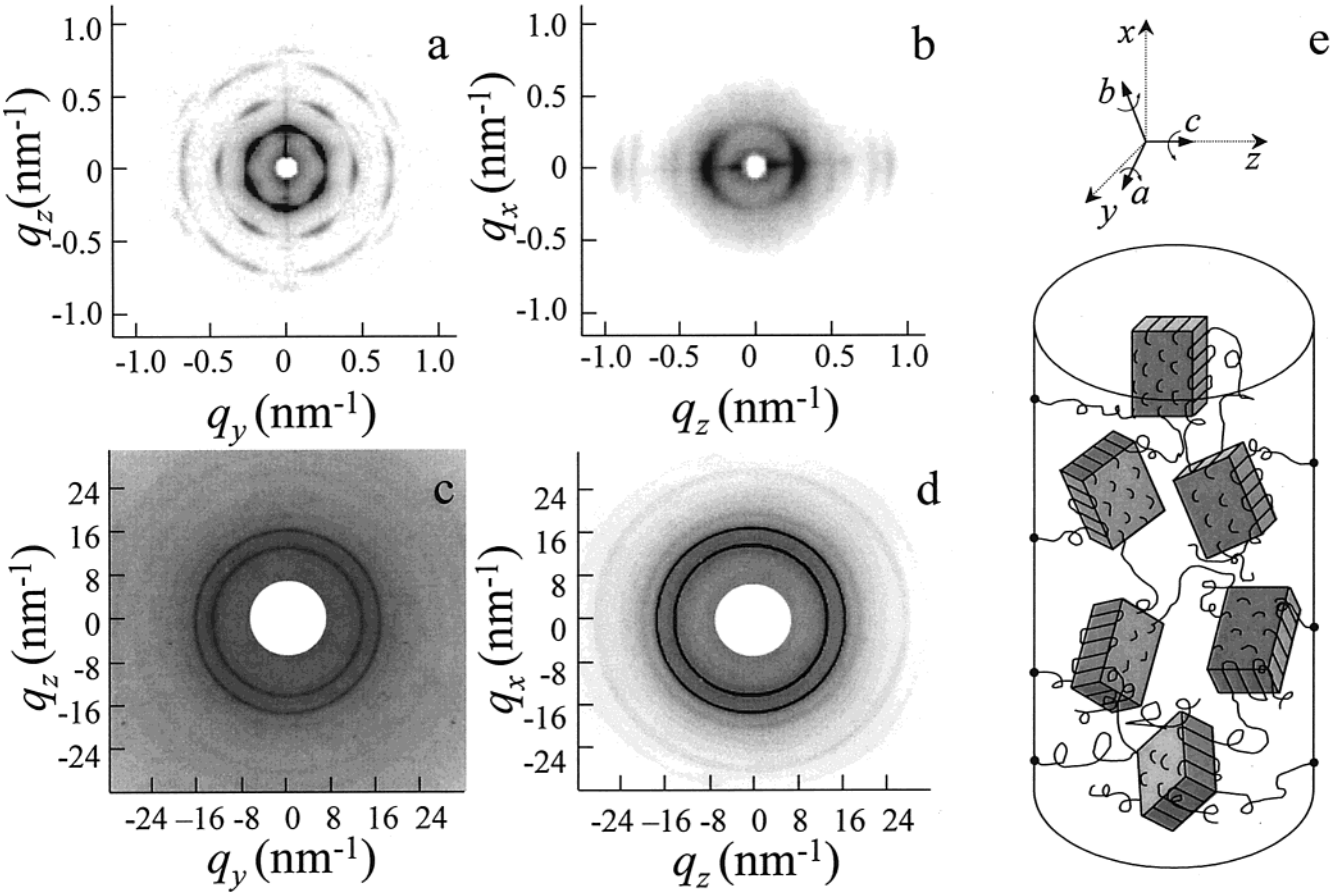

Figure 4. X-ray scattering patterns of shear-aligned sample quickly quenched to $T_c = -50$ °C from 70 °C: (a) a 2D SAXS pattern when the X-ray beam is parallel to *x*; (b) a 2D SAXS pattern when the X-ray beam is parallel to *y*; (c) a 2D WAXS pattern when the X-ray beam is parallel to *x*; (d) a 2D WAXS pattern when the X-ray beam is parallel to *y*; (e) a schematic drawing of randomly oriented PEO crystals within a 2D-confined cylinder in real space.

seen in Figure 3b,c, indicating that the sample obtained from the mechanical shear is not a monodomain hexagonal lattice (or single crystal), and there are polydomains separated by grains, which have orientation distributions around the shear (the *x*) direction. The corresponding 2D WAXS pattern obtained along the *x* direction in Figure 3d shows ring reflections, indicating that the PEO crystal orientation with respect to $\hat{a}$ is isotropic. The 2D WAXS patterns obtained along both the *y* and *z* directions are identical. This kind of observation can also be found for the samples isothermally crystallized at other T_c's. Therefore, only the 2D SAXS and WAXS along the *x* and *y* directions are used in the following discussion of the crystal orientations in nanoconfined cylinders.

Crystal Orientation When $T_c < -30$ °C. After the sample was quickly quenched to a preset T_c, which is below −30 °C, the 2D SAXS and WAXS patterns along the *x*, *y*, and *z* directions are found to be independent upon the T_c in this temperature region. Figure 4 shows a set of 2D SAXS and WAXS patterns of the sample when $T_c = -50$ °C. The SAXS patterns in Figure 4a,b are identical to those in Figure 3a,b, indicating that the cylindrical phase morphology is retained after the sample is isothermally crystallized at −50 °C and the PEO-block crystallization is confined in the nanocylinders. The corresponding 2D WAXS patterns along both the *x* and *y* directions in Figure 4c,d show ring reflections. The inner ring is attributed to the (120) reflection, having a *d*-spacing of 0.463 nm, and the outer ring belongs to the overlapped reflections (*d*-spacing of 0.38−0.40 nm), including the ($\bar{1}$32), (032), (112), ($\bar{2}$12), ($\bar{1}$24), ($\bar{2}$04), and (004) reflections. These results reveal that the PEO crystals are randomly oriented (isotropic) with respect to $\hat{a}$. A real space model is schematically illustrated in Figure 4e. It is deduced that the nucleation density is so high that little crystal growth is needed to complete crystallization due to deep undercoolings. Namely, the PEO crystals are too small to "feel" the 2D cylindrical confinement provided by the PS glassy matrix. On the basis of the diameter size of the cylinders, the PEO crystal size should be sufficiently smaller than 13.7 nm.

Crystal Orientation When Isothermally Crystallized between -30 °C $\leq T_c \leq 0$ °C. 2D SAXS patterns along the *x* and *y* directions (not shown here), obtained after the sample was isothermally crystallized between -30 °C $\leq T_c \leq 0$ °C, are again identical to those in Figure 3a,b, indicating that the cylindrical morphology is preserved after the crystallization of the PEO blocks. The 2D WAXS patterns at $T_c = -30$, -20, -10, and 0 °C are shown in Figure 5a (along the *x* direction) and Figure 5b (along the *y* direction). In Figure 5a, ring reflections again indicate that the *c*-axes of PEO crystals are isotropic with respect to $\hat{a}$ (the *x* direction). However, in each of the 2D WAXS patterns at different T_c's along the *y* direction (Figure 5b), two pairs of the (120) reflections are located in the quadrants and another pair is on the equator, respectively. This indicates that the PEO-crystal *c*-axes are tilted with respect to $\hat{a}$. Here,

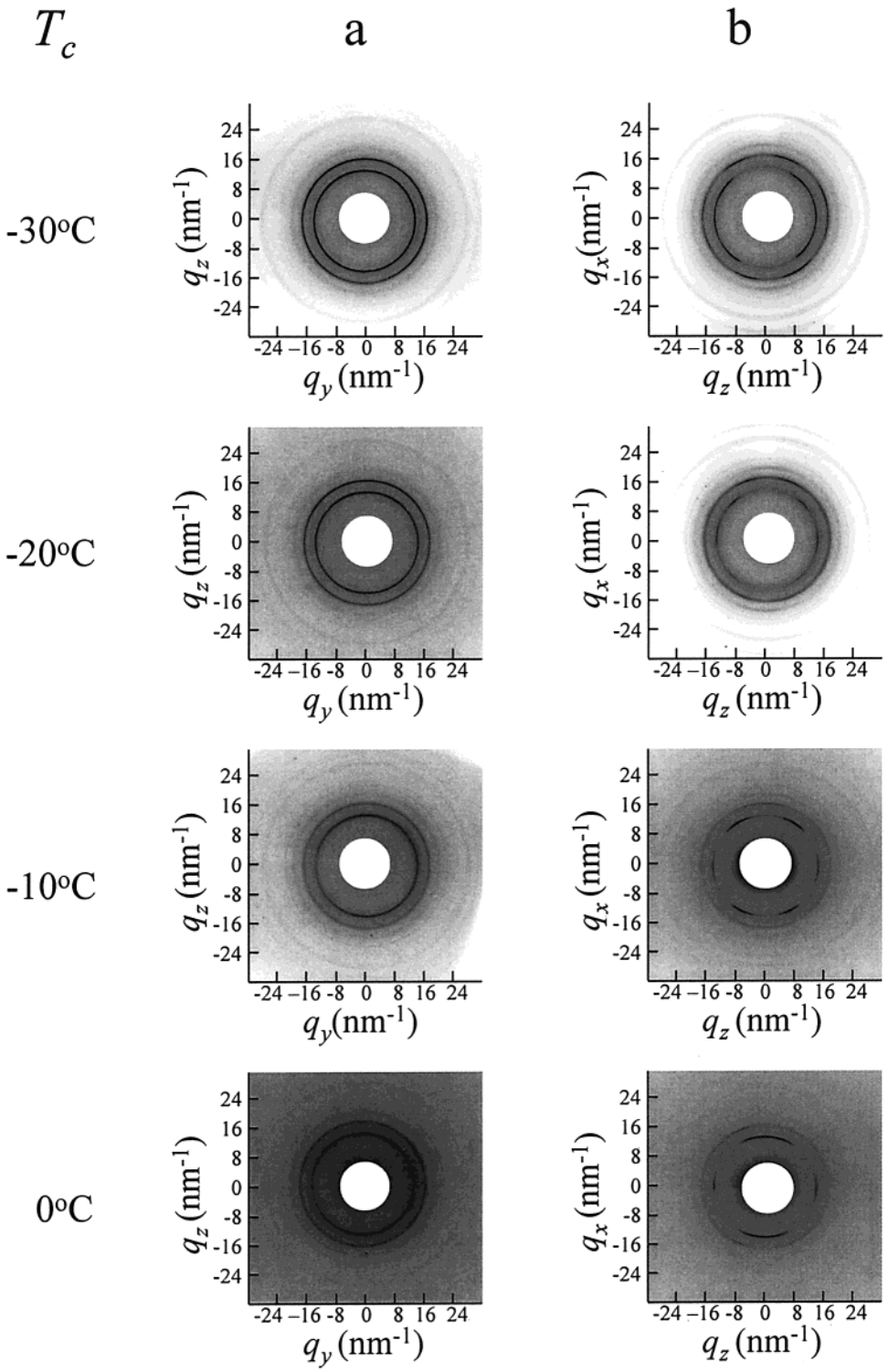

Figure 5. X-ray scattering patterns of shear-aligned samples isothermally crystallized at −30, −20, −10, and 0 °C: (a) 2D WAXS patterns, when the X-ray beam is parallel to *x*; (b) 2D WAXS patterns, when the X-ray beam is parallel to *y*.

we define the tilting angle as an angle between the *c*-axes of the PEO crystals and $\hat{a}$. With increasing T_c, the (120)-reflection pair in the quadrants gradually moves toward the meridian, indicating an increase of the tilting angle away from $\hat{a}$. The tilting angles of crystal *c*-axes are 44°, 48°, and 60° for $T_c = -30$, −20, and −10 °C, respectively. At $T_c = 0$ °C, the (120)-reflection pair in the quadrant almost reaches the meridian in the 2D WAXS pattern. These lead to a broad arc on the meridian (no separated reflections can be clearly identified in the azimuthal scanning profile), suggesting that the tilting angle is close to 90°. An estimation of the tilting angle is around 85°. A relationship between the tilting angle and T_c is plotted in Figure 6.

We use the WAXS pattern at $T_c = -10$ °C (in Figure 5b) as an example for detailed analyses. The predicted $n_{60°}$ uniaxial pattern is shown in Figure 7a, and the predicted and experimentally observed angles between the different reflections and the $n_{60°}$ axis are listed in

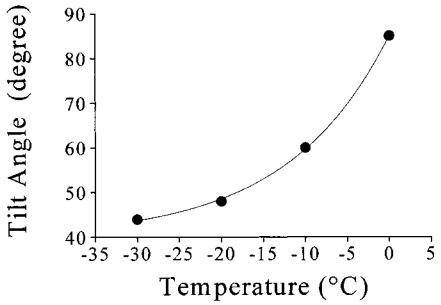

Figure 6. Tilting angle change with T_c in the temperature region of $-30\ °C \leq T_c \leq 0\ °C$.

Table 1. Angles between Different Reflections and the $n_{60°}$ Axis in the $n_{60°}$ Uniaxial Pattern

d-spacing (nm)	reflections	predicted angles with the $n_{60°}$ axis (deg)	obsd angles with the $n_{60°}$ axis (deg)
0.46	$1\bar{2}0$	30, 330	29, 331
	$\underline{1}20$ and $1\bar{2}\bar{0}$	90, 270	89, 273
	$\bar{1}20$	150, 210	148, 211
0.38−0.40	$1\bar{1}2$ and $0\bar{3}2$	25, 335	32, 329
	$\bar{1}\underline{2}4$ and 004	41, 319	
	$1\bar{3}2$, $2\bar{1}2$, $11\underline{2}$, $\bar{1}\bar{3}2$	58, 302	weak
	$0\bar{3}2$ and $21\bar{2}$	80, 280	79, 285
	$\bar{2}04$, $\bar{1}24$, $20\bar{4}$, $1\bar{2}\bar{4}$	90, 270	buried
	$\underline{0}32$ and $\bar{2}\underline{1}2$	100, 260	100, 259
	$\bar{1}32$, $\bar{2}12$, $11\underline{2}$, $13\bar{2}$	122, 238	weak
	$12\underline{4}$ and $00\underline{4}$	139, 221	150, 214
	$\bar{1}\underline{1}2$ and $03\bar{2}$	155, 205	
0.33−0.34	$0\underline{2}4$	14, 346	15, 340
	$2\underline{2}\bar{4}$, $0\underline{2}4$, $\bar{2}\bar{2}4$	72, 288	91, 270
	$\bar{2}\underline{2}4$, $0\underline{2}\bar{4}$, $22\underline{4}$	108, 252	
	$02\underline{4}$	166, 194	164, 199

Table 1. Six (120) reflections are predicted on the first ring (*d*-spacing of 0.463 nm) at 30°, 90°, 150°, 210°, 270°, and 330°. For the 2D WAXS experimental pattern at $T_c = -10$ °C, six maxima are found at 29°, 89°, 148°, 211°, 273°, and 331° on the basis of the azimuthal scanning profiles, which are consistent with the predicted $n_{60°}$ uniaxial pattern in Figure 7a.

On the second ring (*d*-spacing of 0.38−0.40 nm) in Figure 7a, 18 overlapped reflections can be seen, which are attributed to the overlapped (032), ($\bar{1}$32), (112), ($\bar{2}$12), ($\bar{1}$24), ($\bar{2}$04), and (004) reflections, and they are at 25°, 41°, 58°, 80°, 90°, 100°, 122°, 139°, 155°, 205°, 221°, 238°, 260°, 270°, 280°, 302°, 319°, and 335°. For the 2D WAXS pattern at $T_c = -10$ °C, eight maxima at 32°, 79°, 100°, 150°, 214°, 259°, 285°, and 329° can be experimentally observed using the azimuthal scanning profiles. The 32° maximum can be recognized as a merge of two predicted reflections at 25° and 41° in Figure 7a. The predicted reflection of 58° is weak and cannot be observed clearly. Similarly, other observed reflections at around 150°, 214°, and 329° can also be explained as merged reflections. The predicted reflections at 90° and 270° are buried in between adjacent strong reflections at 79° and 100° and at 259° and 285°, respectively.

For the third reflection ring (*d*-spacing of 0.33−0.34 nm) in Figure 7a, eight reflections attributed to the overlapped (024) and ($\bar{2}$24) can be found at 14°, 72°, 108°, 166°, 194°, 252°, 288°, and 346°. For the 2D WAXS pattern at $T_c = -10$ °C, there are six maxima at 15°, 91°, 164°, 199°, 270°, and 340°. The broad reflection maximum at 91° in the experimental observation is due to a merge of two predicted reflections at 72° and 108° in Figure 7a. Similarly, the reflection maximum at around 270° is also resulted from a merge of two predicted reflections at 252° and 288°. Therefore, the experimental 2D WAXS pattern is consistent with the predicted $n_{60°}$ uniaxial pattern in the third reflection ring (Figure 7a).

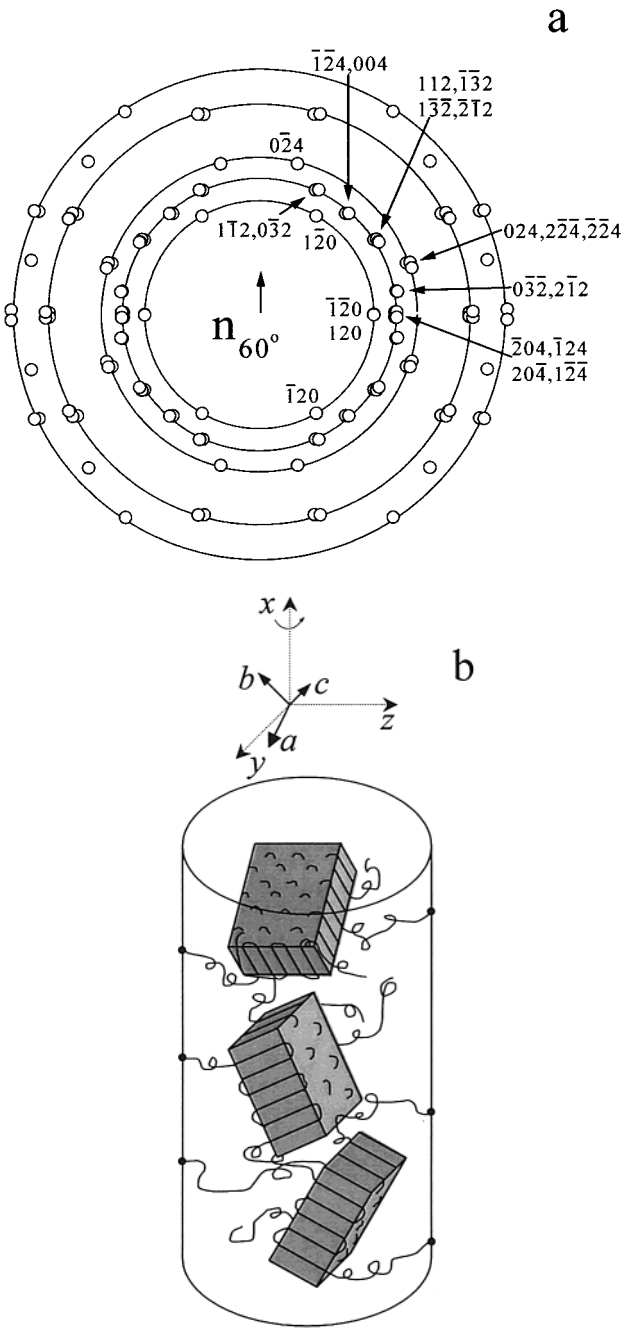

Figure 7. (a) Predicted WAXS tilted $n_{60°}$ uniaxial patterns for PEO crystals. The ($\underline{1}$20) reflections are on the first ring. The ($\bar{1}$32), (032), (112), ($\bar{2}$12), ($\underline{1}\bar{2}4$), ($\bar{2}$04), and (004) reflections are on the second ring. The ($\underline{2}\bar{2}4$) and (024) reflections are on the third ring. The (12$\underline{4}$), ($\bar{3}\underline{2}4$), (044), and ($\bar{2}$44) reflections are on the fourth ring. The ($\bar{1}$08) and ($\bar{3}$08) reflections are located in between the fourth and fifth rings. The ($\bar{3}$28) and ($\bar{1}$28) are on the fifth ring; (b) a schematic drawing of an inclined PEO crystal orientation within a 2D-confined cylinder in real space.

It is important to ensure that the experimentally observed 2D WAXS patterns for the samples crystallized between $-30\ °C \leq T_c \leq 0\ °C$ represent a pure tilted-axis uniaxial crystal orientation rather than a mixture of the tilted-axis and the fiber (*c*-axis uniaxial) patterns. On the basis of the crystallography analyses reported,[15]

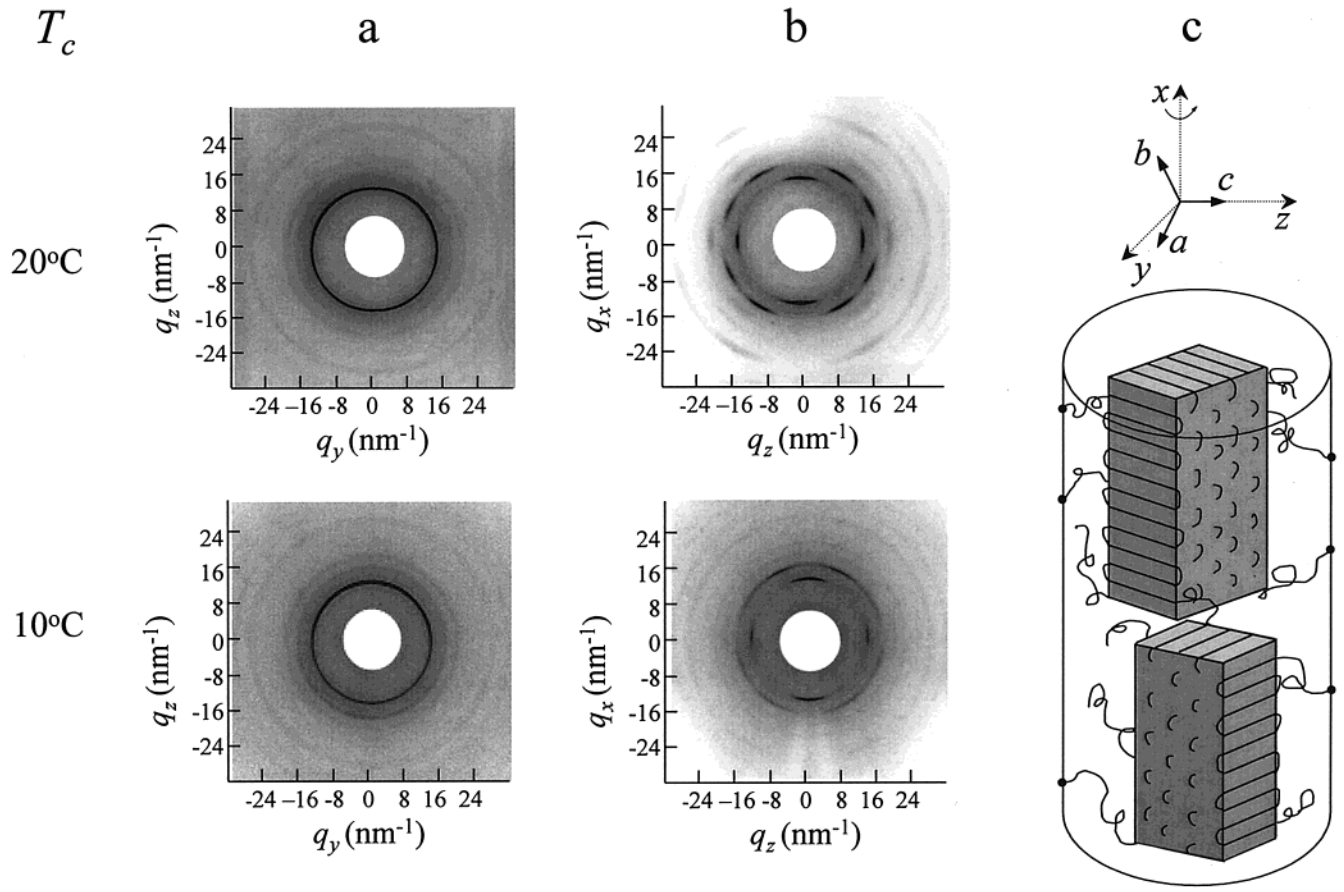

Figure 8. X-ray scattering patterns of the shear-aligned sample isothermally crystallized at 10 and 20 °C: (a) 2D WAXS patterns when the X-ray beam is parallel to *x*; (b) 2D WAXS patterns when the X-ray beam is parallel to *y*; (c) a schematic drawing of perpendicular PEO crystals within a 2D-confined cylinder in real space.

it is known that in the third reflection ring of the PEO fiber pattern (e.g., see Figure 2 in ref 15), reflections at 46°, 134°, 226°, and 314° should be observed.[30−32] Since no strong reflections at these angles are observed in the experiments, we can conclude that the 2D WAXS pattern for $T_c = -10$ °C is a uniform $n_{60°}$ uniaxial pattern. Similar crystallographic analyses can also be carried out for the experimental observations at other T_c's.

We thus conclude that the *c*-axes of the PEO crystals are preferentially oriented inclined to $\hat{a}$ between −30 °C ≤ T_c ≤ 0 °C. The tilting angle increases with increasing T_c. Figure 7b shows a schematic drawing of inclined crystal orientations within a 2D-confined cylinder in real space. The remaining question is why these PEO blocks crystallize into a specifically tilted angle with respect to $\hat{a}$ at each T_c. It is speculated that surface nucleation barriers of the PEO-block crystal growth are affected by the 2D nanoconfined environment. In addition to traditional free energy barriers of the PEO-block crystal growth, an additional positive free energy term may be added to these barriers, and this term could be strongly temperature-dependent. This may provide an exclusive selectivity of the tilted angle in the PEO-block crystallization at each T_c.

Crystal Orientation When Isothermally Crystallized at $T_c \geq 2$ °C. As shown in Figure 6, it can be extrapolated that the tilting angle of the *c*-axes in PEO crystals reaches 90° at $T_c = 2$ °C; namely, the *c*-axes of PEO crystals are perpendicular to $\hat{a}$. The 2D WAXS patterns along both the *x* and *y* directions at $T_c = 10$ and 20 °C are shown in Figure 8a,b (the SAXS and WAXS results of $T_c = 30$ °C are in Figure 3). Experimental 2D SAXS patterns of the sample along both the *x* and *y* directions obtained at $T_c \geq 2$ °C are identical to those shown in Figure 3 ($T_c = 30$ °C), indicating again that the PEO blocks also crystallize within the confined nanocylinders in this T_c region. Figures 8a and 3d show ring reflections in the 2D WAXS patterns along the *x* direction, and therefore, the *c*-axes of PEO crystals are isotropic with respect to $\hat{a}$. The 2D WAXS patterns obtained along the *y* direction in Figures 8b and 3e exhibit that the (120) reflections are located on both the meridian and equator, and the reflection intensities on the meridian are stronger than that on the equator. These patterns can be explained using a [120] uniaxial pattern (see Figure 6 in ref 15). Based on this pattern, four (120) reflections on the first ring (*d* spacing of 0.463 nm) located on both the meridian and equator are predicted. The intensities on the meridian are expected to be stronger than that on the equator because these (120) planes (perpendicular to the meridian) are always parallel to the incident X-ray beam. The experimental reflections in Figures 8b and 3e show four (120) reflections at 0°, 90°, 180°, and 270° and the intensities at 0° and 180° are stronger than those at 90° and 270°, which are consistent with the predicted [120] uniaxial pattern.[15] It has also been found that the (120) reflections on the meridian become sharper with increasing T_c, indicating that the orientation of the PEO crystals improves with increasing T_c. The predicted and experimentally observed angles between the different reflec-

Table 2. Angles between Different Reflections and the [120] Axis

d-spacing (nm)	reflections	predicted angles with the [120] axis (deg)	obsd angles with the [120] axis (deg)
0.46 (first ring)	$1\bar{2}0$ and $\bar{1}\bar{2}0$	0, 180	0, 180
	$1\bar{2}0$ and $\bar{1}20$	90, 270	90, 270
0.38−0.40	$13\bar{2}$,$11\bar{2}$,$21\bar{2}$,$03\bar{2}$	35, 325	34, 327
(second ring)	$12\bar{4}$, $20\bar{4}$, $03\bar{2}$, $2\bar{1}\bar{2}$	65, 295	63, 296
	$00\bar{4}$, $1\bar{2}\bar{4}$, $1\bar{3}2$, $1\bar{1}\bar{2}$		
	$\bar{1}2\bar{4}$, $\bar{1}1\bar{2}$, $0\bar{3}2$, $2\bar{1}\bar{2}$	115, 245	113, 245
	$00\bar{4}$, $\bar{1}2\bar{4}$, $\bar{1}3\bar{2}$, $1\bar{1}\bar{2}$		
	$\bar{1}3\bar{2}$, $\bar{1}1\bar{2}$, $2\bar{1}\bar{2}$, $0\bar{3}\bar{2}$	145, 215	146, 214
0.33−0.34	$22\bar{4}$ and $02\bar{4}$	44, 316	41, 318
(third ring)	$02\bar{4}$, $22\bar{4}$, $0\bar{2}4$, $\bar{2}24$	90, 270	87, 272
	$\bar{2}2\bar{4}$ and $0\bar{2}\bar{4}$	136, 224	134, 225
0.25 (fourth ring)	$24\bar{4}$, $32\bar{4}$, $12\bar{4}$, $04\bar{4}$	36, 324	35, 329
	$04\bar{4}$, $\bar{3}24$, $24\bar{4}$, $\bar{1}2\bar{4}$	75, 285	72, 284
	$0\bar{4}4$, $\bar{3}24$, $2\bar{4}4$, $\bar{1}2\bar{4}$	105, 255	109, 254
	$\bar{2}4\bar{4}$, $\bar{3}24$, $\bar{1}2\bar{4}$, $04\bar{4}$	144, 216	145, 213
0.23[a]	$30\bar{8}$ and $\bar{1}0\bar{8}$	75, 285	69, 296
	$\bar{3}0\bar{8}$ and $10\bar{8}$	105, 255	113, 244
0.21 (fifth ring)	$32\bar{8}$ and $\bar{1}2\bar{8}$	62, 298	90, 270 (br)
	$12\bar{8}$, $3\bar{2}\bar{8}$, $\bar{1}2\bar{8}$, $\bar{3}28$	90, 270	
	$\bar{3}2\bar{8}$ and $12\bar{8}$	118, 242	

[a] There reflections are in between the fourth and fifth rings.

tions and the [120] axis are listed in Table 2. There are eight, six, and eight predicted reflections on the second, third, and fourth reflection rings (*d*-spacing of 0.38−0.40, 0.34−0.33, and 0.25 nm), respectively. By comparing these predicted reflections to experimentally observed angles for the second, third, and fourth rings in Table 2, one can see that the experimental data fits well with the predicted ones.

However, we still need to provide evidence to ensure that the experimentally observed 2D WAXS patterns at $T_c \geq 2$ °C represent a pure [120] uniaxial crystal orientation, rather than a mixture of the [120] uniaxial and the fiber patterns. From the crystallography analyses reported,[15] we know that only the reflections on the fifth ring (*d*-spacing of 0.21−0.22 nm) exhibit differences between the [120] uniaxial and the fiber patterns. This ring is attributed to the $(\bar{1}28)$ and $(\bar{3}28)$ reflections. In the PEO fiber pattern, these reflections are located at $\phi = 28°$, 152°, 208°, and 332°.[30−32] However, only two broad experimental scattering maxima centered at 90° and 270° can be found at $T_c = 30$ °C. We thus conclude that the *c*-axes of PEO crystals are uniformly oriented perpendicular to the $\hat{a}$ of the PEO cylinders for $T_c \geq 2$ °C.

Based on these analyses, a model of the PEO crystal orientation in real space at $T_c \geq 2$ °C can be schematically illustrated in Figure 8c. The *c*-axes of the PEO crystals are perpendicular to $\hat{a}$ and randomly distributed in the *yz* plane. Since one set of the (120) reflections is along $\hat{a}$ (the *x* direction), as shown in Figures 8b and 3e, the 90° crystal orientation with respect to $\hat{a}$ represents the fast crystal growth direction along the [120] in the PEO crystallization,[33,34] which has to conform to $\hat{a}$ in order to maximize crystallinity in the 2D-confined cylinders. Therefore, the *b*-axes of the PEO crystals must tilt 45° from the *x* direction as shown in Figure 8c.

Conclusion

The simultaneous 2D SAXS and WAXS results in a cylinder-forming PS-*b*-PEO/PS blend show that the PEO crystal (the *c*-axis) orientation with respect to the confined cylindrical geometry changes with T_c. Three temperature regions have been recognized which exhibit different crystal orientations: (1) When the sample is quickly quenched to $T_c < -30$ °C from the melt, the *c*-axes of the PEO crystals are randomly oriented within the 2D-confined cylinders. (2) The *c*-axes of the PEO crystals are preferentially oriented inclined to $\hat{a}$ between -30 °C $\leq T_c \leq 0$ °C. Tilting angles between the *c*-axes of PEO and $\hat{a}$ increase with increasing T_c. (3) The *c*-axes of the PEO crystals are preferentially oriented perpendicular to $\hat{a}$ at $T_c \geq 2$ °C. Upon increasing T_c, the crystal orientation gradually improves. This kind of crystal orientation results from the maximum PEO crystal growth along the [120] direction, which is in coincidence with $\hat{a}$.

Acknowledgment. This work was supported by NSF (DMR-9617030). The simultaneous SAXS and WAXS experiments were carried out at the National Synchrotron Light Source at Brookhaven National Laboratory supported by the Department of Energy.

References and Notes

(1) Hirata, E.; Ijitsu, T.; Hashimoto, T.; Kawai, H. *Polymer* **1975**, *16*, 249.
(2) Yang, Y.-W.; Tanodekaew, S.; Mai, S.-M.; Booth, C.; Ryan, A. J.; Bras, W.; Viras, K. *Macromolecules* **1995**, *28*, 6029.
(3) Lotz, B.; Kovacs, A. J. *Kolloid Z. Z. Polym.* **1966**, *209*, 97.
(4) Lotz, B.; Kovacs, A. J.; Bassett, G. A.; Keller, A. *Kolloid Z. Z. Polym.* **1966**, *209*, 115.
(5) Kovacs, A. J.; Lotz, B.; Keller, A. *J. Macromol. Sci., Phys.* **1969**, *B3* (3), 385.
(6) Séguéla, R.; Prud'homme, J. *Polymer* **1989**, *30*, 1446.
(7) Douzinas, K. C.; Cohen, R. E. *Macromolecules* **1992**, *25*, 5030.
(8) Cohen, R. E.; Bellare, A.; Drzewinski, M. A. *Macromolecules* **1994**, *27*, 2321.
(9) Kofinas, P.; Cohen, R. E. *Macromolecules* **1994**, *27*, 3002.
(10) Hamley, I. W.; Fairclough, J. P. A.; Terrill, N. J.; Ryan, A. J.; Lipic, P. M.; Bates, F. S.; Towns-Andrews, E. *Macromolecules* **1996**, *29*, 8835.
(11) Hamley, I. W.; Fairclough, J. P. A.; Ryan, A. J.; Bates, F. S.; Towns-Andrews, E. *Polymer* **1996**, *37*, 4425.
(12) Viras, F.; Luo, Y.-Z.; Viras, K.; Mobbs, R. H.; King, T. A.; Booth, C. *Makromol. Chem.* **1988**, *189*, 459.
(13) Hillmyer, M. A.; Bates, F. S. *Macromol. Symp.* **1997**, *117*, 121.
(14) Hamley, I. W.; Wallwork, M. L.; Smith, D. A.; Fairclough, J. P. A.; Ryan, A. J.; Mai, S.-M.; Yang, Y. W.; Booth, C. *Polymer* **1998**, *39*, 3321.
(15) Zhu, L.; Cheng, S. Z. D.; Calhoun, B. H.; Ge, Q.; Quirk, R. P.; Thomas, E. L.; Hsiao, B. S.; Yeh, F.; Lotz, B. *J. Am. Chem. Soc.* **2000**, *122*, 5957.
(16) Zhu, L.; Chen, Y.; Zhang, A.; Calhoun, B. H.; Chun, M.; Quirk, R. P.; Cheng, S. Z. D.; Thomas, E. L.; Hsiao, B. S.; Yeh, F.; Hashimoto, T. *Phys. Rev. B* **1999**, *60*, 10022.
(17) Zhu, L.; Calhoun, B. H.; Chun, M.; Quirk, R. P.; Cheng, S. Z. D.; Thomas, E. L.; Lotz, B.; Hsiao, B. S.; Yeh, F.; Liu, L. *Macromolecules* **2001**, *34*, 1214.
(18) Quiram, D. J.; Register, R. A.; Marchand, G. R. *Macromolecules* **1997**, *30*, 4551.
(19) Quiram, D. J.; Register, R. A.; Marchand, G. R.; Adamson, D. H. *Macromolecules* **1998**, *31*, 4891.
(20) Liu, L.-Z.; Chu, B. *J. Polym. Sci., Polym. Phys. Ed.* **1999**, *37*, 779.
(21) Park, C.; deRosa, C.; Fetters, L. J.; Thomas, E. L. *Macromolecules* **2000**, *33*, 7931.
(22) Rangarajan, P.; Register, R. A.; Fetters, L. J. *Macromolecules* **1993**, *26*, 4540.
(23) Loo, Y. L.; Register, R. A.; Adamson, D. H. *Macromolecules* **2000**, *33*, 8361.
(24) Jiang, M.; Xie, H. K. *Prog. Polym. Sci.* **1991**, *16*, 977.
(25) Zhu, L.; Mimnaugh, B. R.; Ge, Q.; Quirk, R. P.; Cheng, S. Z. D.; Thomas, E. L.; Lotz, B.; Hsiao, B. S.; Yeh, F.; Liu, L. *Polymer*, in press.
(26) Quirk, R. P.; Kim, J.; Kausch, C.; Chun, M. S. *Polym. Int.* **1996**, *39*, 3.

(27) Zhu, L.; Cheng, S. Z. D.; Calhoun, B. H.; Ge, Q.; Quirk, R. P.; Thomas, E. L.; Hsiao, B. S.; Yeh, F.; Lotz, B. *Polymer* **2001**, *42*, 5847.
(28) Trent, J. S.; Scheinbeim, J. I.; Couchman, P. R. *Macromolecules* **1983**, *16*, 589.
(29) Tepe, T.; Schulz, M. F.; Zhao, J.; Tirrell, M.; Bates, F. S.; Mortensen, K.; Almdal, K. *Macromolecules* **1995**, *28*, 3008.
(30) Takahashi, Y.; Tadokoro, H. *Macromolecules* **1973**, *6*, 672.
(31) Balta Calleja, F. B.; Hay, I. L.; Keller, A. *Kolloid Z. Z. Polym.* **1967**, *209*, 128.
(32) Tadokoro, H.; Chatani, Y.; Yoshihara, T.; Tahara, S.; Murahashi, S. *Makromol. Chem.* **1964**, *73*, 109.
(33) Chen, J.; Cheng, S. Z. D.; Wu, S. S.; Lotz, B.; Wittmann, J.-C. *J. Polym. Sci., Polym. Phys. Ed.* **1995**, *33*, 1851.
(34) Kovacs, A. J.; Straupe, C.; Gonthier, A. *J. Polym. Sci., Polym. Symp. C* **1977,** *59*, 31.

MA010671X